RSC Advances

PAPER

View Article Online
View Journal | View Issue

Cite this: *RSC Adv.*, 2019, **9**, 8169

All-solid-state supercapacitors using a highly-conductive neutral gum electrolyte†

Nengsheng Yu,[abc] Xiaona Wang,[a] Silan Zhang,[a] Sha Zeng,[a] Yongyi Zhang,[ac] Jiangtao Di *[ac] and Qingwen Li[ac]

Received 20th January 2019
Accepted 5th March 2019

DOI: 10.1039/c9ra00494g

rsc.li/rsc-advances

Recently, the development of safe, stable, and long-life supercapacitors has attracted considerable interest driven by the fast-growth of flexible wearable devices. Herein, we report an MnO_2-based symmetric all-solid-state supercapacitor, using a neutral gum electrolyte that was prepared by embedding aqueous sodium sulfate solution in a biopolymer xanthan gum. Resulting from the high ion conductivity 1.12 S m^{-1}, good water retention, and high structure adaption of such gum electrolyte, the presently described supercapacitor showed high electrochemical performance with a specific capacitance of 347 F g^{-1} at 1 A g^{-1} and an energy density of 24 μW h cm^{-2} The flexible supercapacitor possesses excellent reliability and achieves a retaining capacitance of 82% after 5000 cycles. In addition, the as-prepared supercapacitor demonstrated outstanding electrochemical stability at temperatures between −15 °C to 100 °C.

1. Introduction

The ever-growing demands for portable and wearable electronic devices, such as electronic textile, electronic skins, and wearable health monitors, have largely stimulated the rapid development of flexible energy storage devices with excellent electrochemical performance.[1–8] For their practical application, the intrinsic safety issues of flexible and wearable devices needed to be considered seriously because they would undergo the greater mechanical deformation and damage in the process of use. As one of the most popular energy storage devices, in the past century, flexible all-solid-state supercapacitors with a sol–gel electrolyte have attracted much attention for their advantages such as being green and having high power density, long life-time, reliable safety, low cost for fabrication, *etc.*[9] For use in flexible all-solid-state supercapacitors, solid-state ion-conducting composite electrolytes are made of a polymeric material as a matrix and acid, alkaline or salt to provide mobile ions.[10] However, the acid and alkaline electrolyte systems are not environmentally friendly and have generally corrosivity to active materials. Even, it's not safe to the surrounding environment and person once leak occurs during daily use.[11,12] The neutral electrolyte is a superior choose for safety issues of flexible all-solid-state supercapacitor. Among the most neutral electrolyte for supercapacitors, sulfate solutions possess high ionic conductivity and larger voltage window.[13,14] However, the traditional polymer matrixes including PVA,[15] PEO,[16] gelatin,[17] agar,[18] have lower ionic conductivity and the complicated producing process when they were dissolved with neutral or mild salt solutions. Most important, aqueous sulfate ions is easy to precipitate used in the polymers, leading to inferior electrochemical performance. We found xanthan gum have many advantages, including non-toxic,[19] safe[20] and edible polymer, and be used as a thickener and stabilizer in many foods. Moreover, it has high electrical conductivity, electrochemical stability, and chemistry academic stability, and as an electrolyte for wearable equipment, it has good water retention, flexible and easy processing at room temperature.[14]

We report here the use of a neutral gum electrolyte prepared by embedding aqueous sodium sulfate solution in xanthan gum for fabricating flexible MnO_2-based symmetric supercapacitors, which possesses good conductivity, electrochemical stability, and environmental tolerance. Manganese dioxide was electrodeposited onto the CNT films using different the electrochemical deposition voltage to control the morphology. Without using a binder, conductive filler, or any other current collector, the MnO_2/CNT films as positive and negative electrodes could be directly assembled into flexible symmetric supercapacitors, and the devices showed an area capacitance of 347 F g^{-1} at 1 A g^{-1} and the energy density of 24 μW h cm^{-2}. The all-solid-state supercapacitor has good flexural and rate performance and remains 82% after 5000 cycles. Even in extreme environments (−15 °C to 100 °C), the as-

[a]*Key Laboratory of Multifunctional Nanomaterials and Smart Systems, Suzhou Institute of Nano-Tech and Nano-Bionics, Chinese Academy of Sciences, Suzhou, 215123, China. E-mail: jtdi2009@sinano.ac.cn*

[b]*Nano Science and Technology Institute, University of Science and Technology of China, Suzhou 215123, China*

[c]*Division of Nanomaterials, Suzhou Institute of Nano-Tech and Nano-Bionics, Chinese Academy of Sciences, Nanchang 330200, China*

† Electronic supplementary information (ESI) available. See DOI: 10.1039/c9ra00494g

prepared device still maintains excellent electrochemical performance.

2. Experimental section

2.1 Materials

Flexible multi-walled carbon nanotube (CNT) films were prepared by floating catalytic chemical vapor deposition method and were provided by Suzhou Creative Nano Carbon Co., Ltd. Sodium sulfate (Na_2SO_4), manganese acetate ($Mn(CH_3COO)_2$), polyvinyl alcohol (PVA) were analytical reagent and purchased from Aladdin Industrial Co., Ltd. (China). The xanthan gum powder purchased from Aladdin (UPS class).

2.2 Synthesis of MnO_2/CNT film

As-received pristine CNT films were treated by immersing in 12 M HCl and kept at 60 °C for 4 h to make the CNT surface hydrophilic. Manganese dioxide was electrodeposited by a cyclic voltammetry technique in the electrolyte composed of 0.1 M Na_2SO_4 and 0.1 M $Mn(CH_3COO)_2$ at scan rate of 50–250 mV s^{-1} within potential window of 0–1.0 V, using a hydrophilized CNT film as working electrode, a saturated calomel electrode (SCE) as a reference electrode, and a Pt sheet as a counter electrode, respectively. The prepared MnO_2/CNT composite films were then calcined at 200 °C for 10 hours. The mass loading of MnO_2 was measured using a micro balance (Mettler Toledo, model: XP2U).

2.3 Preparation of gum electrolytes

We dissolved 5 g of xanthan gum powder in 50 mL aqueous solution of 1 M Na_2SO_4 solution at room temperature followed by magnetic stirring for 30 min. Then put it in the refrigerator to freeze and keep it crosslinked. The PH of the as-prepared gum electrolyte is about 6.

2.4 Preparation of flexible supercapacitor

Flexible supercapacitors were assembled by using MnO_2/CNT films as both positive and negative electrodes, and Na_2SO_4/xanthan gum was used as both electrolyte and separator. Both positive and negative electrodes were wired by a nickel strip for electrochemical testing. After that, the supercapacitor was sealed by hot-pressing two pieces of polyethylene oxide (PEO) films for encapsulation. The active area of the tested supercapacitor was about 2 × 2 cm^2. The loading mass density of MnO_2/CNT films fabricated at different deposition potential is shown in Table S1.†

2.5 Materials characterization

Morphology characterization of the investigated samples was performed using a scanned electronic microscope (SEM) (Quanta 400 FEG, FEI) and transmission electron microscope (TEM) (Tecnai G2 F20 S-Twin, FEI). The Raman spectrum was measured by a laser confocal Raman microscopy (Lab RAM HR, HORIBA Jobin-Yvon). The thermo-gravimetric analysis was executed by thermogravimetry (TG 209F1, NETZSCH, Germany). The XRD data were collected by D8 Advance Powder X-ray diffractometer (Bruker AXS). The infrared spectrum is measured by micro-infrared absorption spectrometer (IR Nicolet iN10).

2.6 Electrochemical measurement

Cyclic voltammetry and electrochemical impedance spectroscopy were conducted on a CHI 660 C potentiostat. Impedance measurements were carried out between 10 kHz to 0.01 Hz with an AC amplitude of 10 mV. A piece of gum was placed between two stainless sheets of steel having an area of 4 cm^2, and then the gum was uniformly compressed into a 0.21 cm-thick film. The real impedances at the highest frequency were taken as the bulk resistance. The charge/discharge measurements were carried out on a LANHER battery tester (Wuhan). The capacitance, energy density, and power density were calculated based on the mass of MnO_2. The specific capacitance of supercapacitor was calculated by

$$C = \frac{I\Delta t}{m\Delta V}. \quad (1)$$

The energy density (E) of supercapacitor was calculated by

$$E = \frac{CV^2}{2}, \quad (2)$$

and the power density (P) was calculated by

$$P = \frac{E}{t}. \quad (3)$$

where t (s) is the discharge time, m (g) is the mass of the active materials in the electrodes, ΔV (V) is the range of potential, I (A) is the discharge current.

3. Results and discussion

3.1 Basic properties of xanthan gum electrolyte

Xanthan gum is an important commercial polysaccharide, which is non-toxic, low-cost and widely used as food additives.[21] It has very high salt tolerance. As shown in Fig. S1,† the gum electrolyte containing 20 wt% of xanthan gum remained highly stable even after adding 3 M of Na_2SO_4. In contrast, aqueous polyvinyl alcohol solution was salted out after adding 0.1 M of Na_2SO_4. Fig. 1a shows some hand-made shapes of xanthan gum. It can also be wound around a thin steel bar. These observations indicated that the prepared gum electrolyte was highly sticky, shapeable and stable, which could facilitate the utilization of such electrolyte for preparing flexible supercapacitors.

Fig. S2† shows the Nyquist plots obtained from gum electrolytes that were prepared by dissolving xanthan in Na_2SO_4 solutions with concentrations of 0.1 M, 0.5 M, 1 M, 2 M and 3 M, and the extracted ionic resistance as a function of Na_2SO_4 concentration was plotted in Fig. 1b. It indicates that the ionic conductivity of the gum electrolytes increased with the Na_2SO_4 concentration and reached the maximum of 1.36 S cm^{-1} at 3 M. The conductivity of supercapacitor electrolyte with 1 M sodium sulfate concentration reached 1.12 S m^{-1}, the resulted

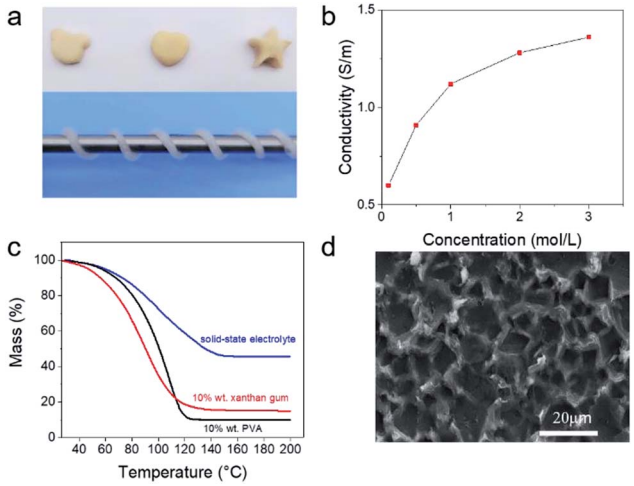

Fig. 1 (a) Photographs of hand-made various shapes of xanthan gum electrolytes; (b) ionic conductivity of different concentrations of Na_2SO_4/xanthan gum electrolytes; (c) TGA curves of different gel electrolytes; (d) SEM image of the xanthan gum.

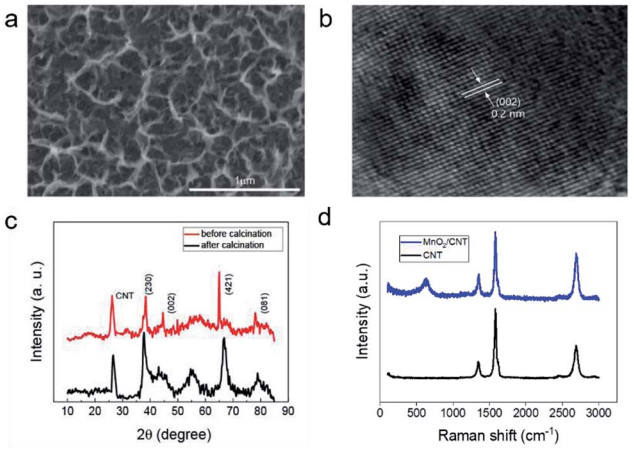

Fig. 2 (a) SEM image of the MnO_2-3a synthesized by CV electrodeposition; (MnO_2-3a: 0.3–1.0 V 250 mV s^{-1}) (b) The HRTEM images of MnO_2; (c) XRD spectra of MnO_2-3a/CNT films; (d) Raman spectra of MnO_2-3a/CNT films.

conductivity is much higher than the results for commonly used aqueous gel electrolytes such as KOH/PVA, LiCl/PVA.[22–24]

To understand the water retention ability of such electrolytes, we performed thermogravimetric analysis on three solutions that were PVA gel, xanthan gum and Na_2SO_4/xanthan gum electrolytes, respectively. The results are shown in Fig. 1c. The initial water content of the three gel electrolytes is 90%, 90%, and 65%, respectively. At temperatures above 100 °C, water weight percentages were almost zero for the PVA gel but about 6.5% and 12% for the pristine xanthan gum and the Na_2SO_4/xanthan gum electrolyte, respectively. These comparisons indicate that the xanthan gum has very strong water retention. Importantly, the water retention of the Na_2SO_4/xanthan gum electrolyte was higher than that of pure xanthan gum. There are probably two main reasons: first, after adding salt, more water can be locked in the molecular transition which can be confirmed by the infrared spectra shown in Fig. S3.†[25–28] The characteristic peaks of hydroxyl groups on carboxyl groups become wider, illustrating that metal cations in salts replace hydrogen ions in carboxylic acids of xanthan gum to maintain a more stable conformation of xanthan gum.[29] Then, the water in the electrolyte can be converted to the bound water in the salt with temperature increase. Scanning electron microscopy indicates that the gum electrolyte has a porous structure (Fig. 1d). This structure can facilitate the transport of electrolyte and reservation of aqueous electrolyte.

3.2 Basic properties of MnO_2/CNT film

MnO_2 nanostructure was deposited on the CNT film under different potential windows using a cyclic voltammetry method. The morphologies of MnO_2 deposited in the different conditions are shown in Fig. 2a and S4.† We tested the electrochemical performance of these electrodes. Fig. S5a–d† shows the electrochemical results of MnO_2/CNT films obtained in 1 M Na_2SO_4 electrolyte using investigated samples as the working electrode, SCE as the reference electrode and a Pt wire as the counter electrode, respectively. Fig. S5a† shows the *CV* curves of MnO_2 under different deposition potential window at a scan rate of 5 mV s^{-1}, MnO_2-3 possess the largest specific capacitance, illustrating it has better electrochemical properties than other samples. Fig. S5b† shows that *CV* curves of MnO_2-3 at a different scan speed of 50 mV s^{-1}, 100 mV s^{-1} and 250 mV s^{-1}. The largest specific capacity can be obtained when MnO_2-3a was implemented at the scan rates of 250 mV s^{-1}. The GCD curves of MnO_2-3a in Fig. S5c† exhibits that discharge curves were almost symmetrical to the corresponding charge curves, indicating good capacitive behavior of the MnO_2-3a/CNTs. The specific capacitances in Fig. S5d† were calculated based on Fig. S5c† and eqn (1) at different current density. The MnO_2-3a/CNT electrode maintained a capacitance of 71.1% of original capacitance at a current density of 10 A g^{-1}, illustrating that MnO_2-3a has good rate performance. Detailed microstructural of MnO_2-3a was investigated by SEM and is shown in Fig. 2a, exhibiting a multistage structure consisting of nanosheets and nanopores. This structure is beneficial to the diffusion of electrolyte ion during the charge and discharge process. In addition, this structure has a larger specific surface area, which enables adsorb and store more ions and enhance the ion transport, thus improving the capacitance of capacitors. The internal lattice of manganese oxide synthesized in liquid state contains a large amount of crystalline water and there's also some water in the multistage porous structures lost at 200 °C (Fig. S6†). The mass of MnO_2 decreases between 300 °C and 400 °C due to the transformation of γ-MnO_2 to β-MnO_2. Mass degradation at more than 400 °C is mainly due to oxidation etching of carbon films in air and partial decomposition of manganese oxide at high temperatures. Based on the results of TG, the annealed MnO_2 was characterized by high resolution TEM (HRTEM). As shown in Fig. 2b, the lattice fringes of MnO_2 were clear, indicating that the crystallinity of MnO_2 was good. The lattice spacing is 0.2 nm, which can be deduced that the corresponding crystal plane is (002). The MnO_2/CNT before and after

annealing were characterized by XRD as shown in Fig. 2c. The diffraction peaks of the MnO_2/CNT before annealing at 2θ of 38°, 44°, 68°, and 78° is corresponding to (230), (002), (421), and (081) planar reflections of γ-MnO_2 standard pattern, respectively, which is consistent with the characterization results of HRTEM. But, after annealing, the strength of characteristic peaks increases obviously, and the width of half height becomes narrower, which indicates that annealing treatment improves the crystallinity. Raman spectroscopic results shown in Fig. 2d and S7† reveals that Mn–O resonance peaks in [MnO_6] octahedron at 641 cm^{-1}.

3.3 Electrochemical test of all-solid-state supercapacitors

To evaluate the electrochemical properties of all-solid-state supercapacitors, CV and GCD tests were carried out using a two-electrode system in 1 M Na_2SO_4/xanthan gum. A symmetrical flexible all-solid-state supercapacitor was assembled using a pair of MnO_2-3a/CNT films as positive and negative electrodes (shown in Fig. 3a). Fig. 3b displays the *CV* curves of flexible all-solid-state supercapacitor at different scan rates from 1 to 100 mV s^{-1} in a potential window of 0–1 V. The symmetrical quasi-rectangular shape of *CV* curves disclose the ideal capacitive behaviours of the all-solid-state supercapacitors. Moreover, such a quasi-rectangular shape is well retained even at the scan rate up to 100 mV s^{-1}, indicating good high-rate performance. As a comparison, symmetrical supercapacitors assembled using pristine films as electrodes showed much lower capacitance than the MnO_2/CNT-based supercapacitor. This indicate that the capacitance was mainly contributed by the deposited MnO_2 layer (Fig. S8 in the ESI†). During the charge and discharge process, redox reaction of $MnO_2 + Na^+ + e^- = MnOONa$ was favorable in a voltage range from 0 V to 1 V. Also, for the MnO_2-3a/CNT film, the shape encased by a redox curve at a high scan rate, indicating the good reversibility of MnO_2/MnOONa reaction occurred on CNT film.[30,31] The MnO_2 electrode in mild aqueous electrolyte, fast surface redox reactions define the behaviour of the voltammogram, whose shape is close to that of the EDLC. So it is hard to observe the evident redox peak on the *CV* curves.[32] Except for CV measurement, the charge–discharge curves exhibit the nearly symmetric feature with small IR drop (Fig. 3c), also suggesting excellent electrochemical capacitive characteristics and reversible faradaic reaction between Na^+ and MnO_2-3a/CNT films. The near-ideal triangular shape of the GCD curves suggests a fast charge–discharge process, which is in good agreement with the results of the CV tests. The as-prepared device possesses a high capacitance of 347 F g^{-1} at a small current density 1 A g^{-1} and 128.8 F g^{-1} at a large current density of 10 A g^{-1} (Fig. 3d). In addition, we can see that the coulombic efficiency is poor in the first 10 cycles at current density of 1 A g^{-1}, but it gets better at last 10 cycles. It may be because the internal ion transport channel of the MnO_2-3a/CNT films is incomplete in the first 10 cycles, and MnO_2 is activated after charging and discharging for many times, thus making its coulombic efficiency higher. Such a high special capacitance of the MnO_2-3a/CNT film electrode should be attributed to the large surface area of active materials and high ion conductivity of the electrolyte, which endow more active sites for electrochemical reaction and fast electron transport. The Ragone plots of the flexible supercapacitors calculated from charge/discharge curves are shown in Fig. S9.† The device composed MnO_2/CNT shows highest energy densities (around 24–46 μW h cm^{-2}) with the increase of power densities from 0.1 to 2.3 mW cm^{-2}, which is higher than the values reported for flexible supercapacitors based on other MnO_2 composite electrodes.[32,35–37] Also, long cycling test and electrochemical impedance spectroscopy (EIS) measurement are performed to explore the electrochemical stability of the all-solid-state supercapacitors. Fig. 3e shows that coulombic efficiency remain around 100% throughout 10 000 charging/discharging cycles, indicating a very good cyclic stability for our supercapacitors. In initial 2000 cycles, capacitance gradually drops from 100% (347 F g^{-1}) to 94.3% (327.3 F g^{-1}) which keep capacity about 82% of original capacity in 5000 cycles, was superior than most of the MnO_2 based flexible electrodes.[33,34] Then, that the specific capacitance of device after 10 000 cycles is kept to 67.1% at charge/discharge current density of 1 mA cm^{-2}. This capacity fading should be attributed to the dissolving of MnO_2 into soluble Mn^{2+} ions. According to Nyquist plots of the capacitor after 10 000 cycles, the charge-transfer resistance increases from 4 Ω to 8 Ω, leading to decline in electrolyte conductivity (Fig. S10†). This may be because electrolyte was drying during electrochemical reaction process.

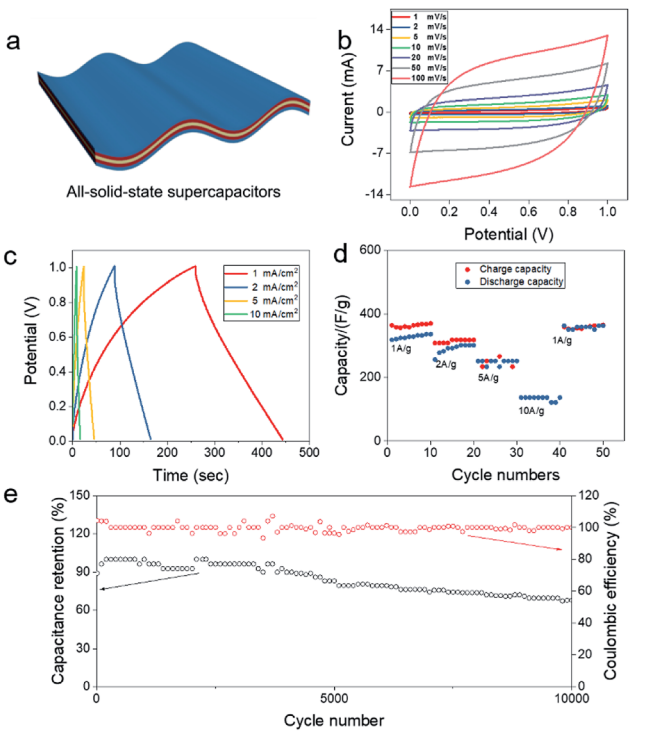

Fig. 3 (a) The scheme of subsequent preparation of all-solid-state supercapacitors; (b) *CV* curves of all-solid-state supercapacitor at different scan rates; (c) GCD curves of all-solid-state supercapacitors at different current density; (d) rate performance of all-solid-state supercapacitor at different current density; (e) cycle performance of all-solid-state supercapacitors.

3.4 Electrochemical performance of all-solid-state supercapacitors at different temperatures

In order to estimate the electrochemical properties of all-solid-state supercapacitors in server environment, we put all-solid-state supercapacitors into a thermostat to simulate the external temperature. As shown in Fig. 4a, the *CV* curves of all-solid-state supercapacitors in a two-electrode system at different temperatures at the scan rate of 2 mV s^{-1} maintain similar shapes, illustrating that supercapacitors have good environmental tolerance. However, we can find that current density is higher at high temperature than that at low temperature, which may be due to the fact that redox reaction is easier to carry out at a high temperature. Also, the *CV* curves display that capacitance at high temperatures is higher than that at low temperatures. According to the Brownian motion law, the rate of ion transport at high temperature is more active than that at low temperature, making the electrochemical reaction is easier. Fig. 4b shows Nyquist plots of the capacitor at a different temperature, hydraulic resistance at high temperatures is smaller than that at low temperatures, demonstrating the capacitance at high temperatures is higher than that at low temperatures. It can't be salted out even at low temperatures or dissolve at high temperatures, making the devices work normally at different temperatures. These results also demonstrated that xanthan gum possesses the stable physical properties that can resist high and low temperatures.

3.5 Electrochemical performance of all-solid-state supercapacitors at different bent state

We further demonstrated the practical application of as-prepared all-solid-state supercapacitors. Fig. 5a displays the utilization of the as-prepared flexible supercapacitor to power an electric time meter. As shown in Fig. 5b, to examine the flexibility and mechanical stability of all-solid-state supercapacitors, GCD curves of all-solid-state supercapacitors was carried out at 1 mA cm^{-2} under different bending states. The corresponding GCD curves keep almost no change under bending states, revealing excellent bendability and mechanical stability. Moreover, after bending for 100 cycles at state 2, the specific capacity of all-solid-state supercapacitor remained 93% of the initial value. Such findings suggest that the high flexibility of our flexible all-solid-state supercapacitors, which is of great importance for the applications of such supercapacitors in wearable devices.

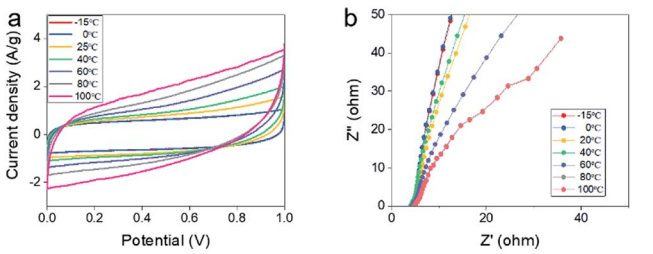

Fig. 4 Electrochemical test of all-solid-state supercapacitors in a two-electrode system at different temperatures. (a) *CV* curves at the scan rate of 2 mV s^{-1}; (b) Nyquist plots with a frequency range of 100 kHz to 0.01 Hz.

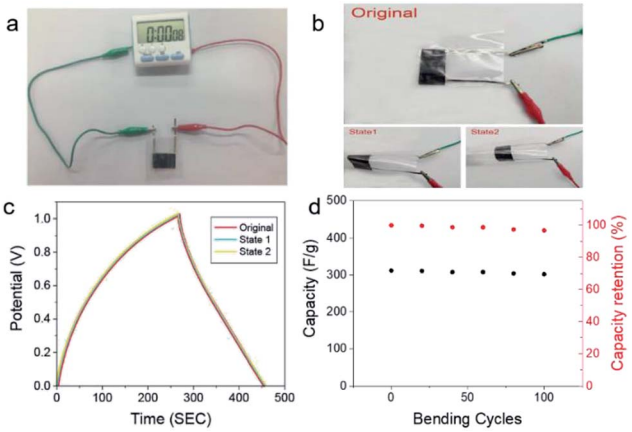

Fig. 5 (a) Optical image of flexible as-assembled symmetric supercapacitor power an electric time meter; (b) optical images of all-solid-state supercapacitors at different bent state; (c) GCD curves of all-solid-state supercapacitors at different bent state; (d) specific capacitances (right axis) and capacity retention (left axis) as a function of bending cycles for the supercapacitors.

4. Conclusions

In summary, we use MnO_2/CNT as positive and negative electrodes and Na_2SO_4/xanthan gum as a solid electrolyte to assemble all-solid-state supercapacitor. Xanthan gum has better electrochemical properties and environmental temperature tolerance than ordinary electrolyte used in flexible energy storage devices. The Na_2SO_4/xanthan gum electrolyte has good flexibility, mechanical strength, high conductivity, good water retention and can be prepared easily at room temperature. All-solid-state supercapacitor has a superior specific capacitance of 347 F g^{-1} at 1 A g^{-1} and energy density of 24 μW h cm^{-2} even when the power density was increased to 2.3 mW cm^{-2}. The flexible supercapacitor possesses excellent reliability and achieves a retaining capacitance of 82% after 5000 cycles. In addition, it shows stable electrochemical performance in both planar and bent status. Meanwhile, all-solid-state supercapacitors also exhibit excellent electrochemical stability at temperatures between −15 °C to 100 °C. Such, lighten, flexible and high ionic conductive xanthan gum electrolyte boosts the practical application for next-generation flexible wearable energy storage devices in the future.

Conflicts of interest

There are no conflicts to declare.

Acknowledgements

This work was supported by the National Key Research and Development Program of China (2016YFA0203301), the National Natural Science Foundation of China (21773293,

21603264, 51602339), CAS Pioneer Hundred Talents Program (J. Di), Key Research Program of Frontier Science of Chinese Academy of Sciences (QYZDB-SSW-SLH031), and the Science and Technology Project of Nanchang (2017-SJSYS-008), the Natural Science Foundation of Jiangsu Province, China (No. BK20160399), the Postdoctoral Foundation of China (No. 2016M601905), Jiangsu Planned Projects for Postdoctoral Research Funds (No. 1601065B).

Notes and references

1 Q. Huang, D. Wang and Z. Zheng, *Adv. Energy Mater.*, 2016, **6**, 1600783.
2 L. Dong, C. Xu, Y. Li, C. Wu, B. Jiang, Q. Yang, E. Zhou, F. Kang and Q.-H. Yang, *Adv. Mater.*, 2016, **28**, 1675–1681.
3 Y. Ai, Z. Loua, S. Chena, D. Chen, Z. M. Wang, K. Jiangd and G. Shen, *Nano Energy*, 2017, **35**, 121–127.
4 X. Pu, M. Liu, X. Chen, J. Sun, C. Du, Y. Zhang, J. Zhai, W. Hu and Z. L. Wang, *Sci. Adv.*, 2017, **3**, e1700015.
5 Y. Liu, M. Phar and G. A. Salvatore, *ACS Nano*, 2017, **11**, 9614–9635.
6 Y. Khan, A. E. Ostfeld, C. M. Lochner, A. Pierre and A. C. Arias, *Adv. Mater.*, 2016, **28**, 4373–4395.
7 L. Li, Z. Wu, S. Yuan and X.-B. Zhang, *Energy Environ. Sci.*, 2014, **7**, 2101–2122.
8 L. Peng, Y. Zhu, H. Li and G. Yu, *Small*, 2016, **12**(45), 6183–6199.
9 X. Peng, L. Peng, C. Wu and Y. Xie, *Chem. Soc. Rev.*, 2014, **43**, 3303.
10 Y. Shao, M. F. El-Kady, J. Sun, Y. Li, H. Wang, B. Dunn and R. B. Kaner, *Chem. Rev.*, 2018, **118**, 9233–9280.
11 E. Verlage, S. Hu, R. Liu, J. Ryan, R. Jones, K. Sun, C. Xiang, S. L. Nathan and A. A. Harry, *Energy Environ. Sci.*, 2015, **8**, 3166–3172.
12 C. Zhong, Y. Deng, W. Hu, J. Qiao, L. Zhang and J. Zhang, *Chem. Soc. Rev.*, 2015, **44**, 7484–7539.
13 J. Le Bideau, J. B. Ducros, P. Soudan and D. Guyomard, *Adv. Funct. Mater.*, 2011, **21**, 4073.
14 S. Zhang, N. Yu, S. Zeng, S. Zhou, M. Chen, J. Di and Q. Li, *J. Mater. Chem. A*, 2018, **6**, 12237–12243.
15 X. Peng, H. Liu, Q. Yin, J. Wu, P. Chen, G. Zhang, G. Liu, C. Wu and Y. Xie, *Nat. Commun.*, 2016, **7**, 11782.
16 S.-H. Bae, C. Jeon, S. Oh, C.-G. Kim, M. Seo and Il-K. Oh, *Carbon*, 2018, **139**, 10–20.
17 A. Railanmaa, S. Lehtimäki and D. Lupo, *Appl. Phys. A*, 2017, **123**, 459.
18 W. G. Moon, G.-P. Kim, M. Lee, H. D. Song and J. Yi, *ACS Appl. Mater. Interfaces*, 2015, **7**, 3503–3511.
19 M. Zhenga, F. Lian, Y. Xiong, B. Liua, Y. Zhua, S. Miao, L. Zhang and B. Zheng, *Food Chem.*, 2019, **272**, 574–579.
20 J. Fan, K. Wang, M. Liu and Z. He, *Carbohydr. Polym.*, 2008, **73**, 241–247.
21 N. B. Wyatt and M. W. Liberatore, *Soft Mater.*, 2010, **6**, 3346.
22 J. Fu, J. Qiao, H. Lv, J. Ma, X.-Z. Yuan and H. Wang, *ECS Trans.*, 2010, **25**, 15–23.
23 W. Fu, E. Zhao, X. Ren, A. Magasinski and G. Yushin, *Adv. Energy Mater.*, 2018, **8**, 1703454.
24 L. Zhi, C. Yang, T. Li, H. Zhang and F. Huang, *Nanoscale*, 2016, **8**, 4054–4062.
25 M. A. Zirnsak, D. V. Boger and V. Tirtaatmadja, *J. Rheol.*, 1999, **43**, 627–650.
26 M. Milas, W. F. Reed and S. Printz, *Int. J. Biol. Macromol.*, 1996, **18**, 211.
27 T. Sho, S. Kojima and T. Norisurye, *Polym. J.*, 1986, **25**, 307.
28 T. Sho, T. Sato and T. Norisurye, *Biophys. Chem.*, 1986, **25**, 307.
29 F. Lai, J. Feng, R. Yan, G.-C. Wang, M. Antonietti and M. Oschatz, *Adv. Funct. Mater.*, 2018, **28**, 1801298.
30 Y. Wang, Y.-Z. Zhang, D. Dubbink and J. E. ten Elshof, *Nano Energy*, 2018, **49**, 481–488.
31 G. Huang, Y. Zhang, L. Wang, P. Sheng and H. Peng, *Carbon*, 2017, **125**, 595–604.
32 P. Simon and Y. Gogotsi, *Nat. Mater.*, 2008, **8**, 845–854.
33 H. Chen, S. Zeng, M. Chen, Y. Zhang, L. Zheng and Q. Li, *Small*, 2016, **12**(15), 2035–2045.
34 S. D. Perera, M. Rudolph, R. G. Mariano, N. Nijem, J. P. Ferraris, Y. J. Chabal and K. J. Balkus, *Nano Energy*, 2013, **2**, 966–975.
35 Y. He, W. Chen, X. Li, Z. Zhang, J. Fu, C. Zhao and E. Xie, *ACS Nano*, 2013, **1**, 174–182.
36 Q. Cheng, J. Tang, J. Ma, H. Zhang, N. Shinya and L.-C. Qin, *Carbon*, 2011, **49**, 2917–2925.
37 Z. Lv and X. Chen, *Adv. Mater.*, 2018, **30**, 1704531.